# POLITECNICO DI TORINO
## Repository ISTITUZIONALE

Thermomechanical calibration of FBG sensors for aerospace applications

(Article begins on next page)

16 May 2024

# Thermomechanical calibration of FBG sensors for aerospace applications

*Alessandro Aimasso\*[†],Matteo D.L. Dalla Vedova\*, Paolo Maggiore\**
*Department of Mechanical and Aerospace Engineering*
*Politecnico di Torino, Itaky*
alessandro.aimasso@polito.it – matteo.dallavedova@polito.it – paolo.maggiore@polito.it
[†] Corresponding Author

**Abstract**
Optical fibers have found widespread use in engineering, from communication to sensors. Among them, Fiber Bragg Gratings are allowed to detect several parameters. Scope of this work is to assess their performances as temperature and mechanical strain sensors for aerospace: in this regard, an experimental calibration is discussed. Then, alternative approaches are tested in order to distinguish thermal from mechanical contributes. This is first addressed by using a hybrid system of digital and optical sensors, and then then with a fully optical system. Both the presented solutions reached the scope. A concept of a third, innovative approach, is also described.

## 1. Introduction

Optical fiber is a well-established technology in the telecommunications sector [1], which has brought about one of the most significant technological revolutions in recent decades. However, its unique physical properties have also made it highly appreciated for sensing applications. In modern and frontiers engineering projects, it is increasingly important to have sensors that can provide high performance even in harsh environments, a typical requirement in the aerospace industry as well. Fiber optics can meet this requirement, particularly in terms of its immunity to electromagnetic interference and its ability to operate in both cryogenic and extremely high temperatures [2]–[7]. Over the past years, several studies have been conducted at the Politecnico di Torino to integrate fiber optic technology into aerospace system components [8]–[11].

In addition to the wide operating temperature range and immunity to electromagnetic interference, optical fiber based sensors offer, among his features, minimal invasiveness to the instrumented component, the ability to accommodate multiple sensors on the same communication line and the capability to monitor explosive environments due to its chemical inertness. All these properties enable the integration of fiber optics directly into the monitored component, providing a multifunctional, innovative, and smart approach to prognostics, diagnostics, and system health monitoring [12]–[14]. Moreover, and crucially for the work conducted in this study, the same instrumentation can monitor vastly different physical parameters [15]–[19].

The purpose of this paper is precisely to evaluate the capability of a fiber optic system to monitor a specific physical parameter, even when subject to the simultaneous effects of multiple factors: in fact, the cross-sensitivity to environmental factors could be a limit for its application [20], [21].

## 2. Optical fiber and FBG sensors

An optical fiber typically has a cylindrical shape made up of numerous concentric layers. The one with the largest diameter, between 5 and 50 μm, is referred to as the core and has a refractive index of $n_1$. A final protective layer, the coating, is added to protect the structure from potential damages brought on by the fiber's incredibly low bending resistance. It is placed on top of the cladding, an outer layer that is appropriately doped to achieve a refractive index of $n_2 > n_1$ with a thickness of 125 μm. Several extra outside layers could be added to increase mechanical strength because to its severe fragility.
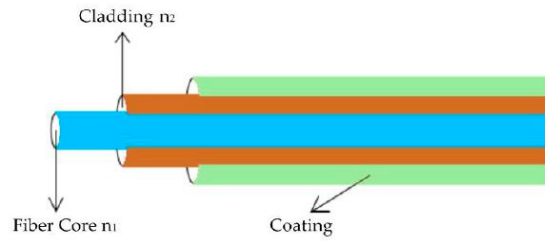
Figure 1: optical fiber structure

The signal transmission process within the fibre obeys the principle of total reflection. In fact, since the refractive index of the core $n_1$ is greater than that of the cladding $n_2$, according to *Snell's Law*:

$$n_1 sin\theta_1 = n_2 sin\theta_2 \tag{1}$$

where:
- $\theta_1$ is the angle of incidence.
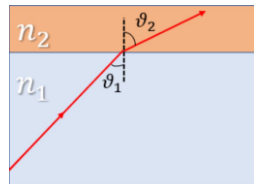- $\theta_2$ is the refraction angle.



Figure 2: scheme of Snell's Law

It turns out that for an angle of incidence $\theta_1$ greater than:

$$\theta_c = \arcsin\frac{n_2}{n_1} \tag{2}$$

the light beam introduced into the core will undergo total reflection at the interface between core and cladding, resulting confined within the optical fiber and allowing the signal transmission. This condition is always verified in optical fibers.
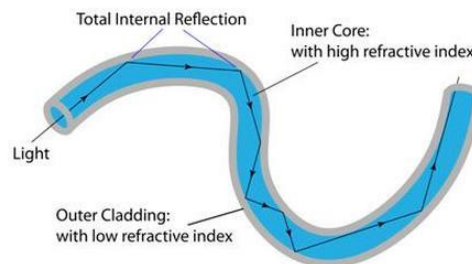


Figure 3: optical fiber signal conduction

Optical fiber can only transmit signals. Fiber Bragg Gratings (FBG) sensors can be used as a sensor for mechanical deformations and temperature variations. There are various benefits from using them:

- They are unobtrusive due to their light weight and small size;
- They do not require electricity to work;
- They may be easily integrated into composite materials during the lamination step, as well as bonded to the surface, as conventional sensors are;
- They can also be used in severely stressed structures;
- A large number of sensors can be put on a single optical line.

They do, however, come with a number of disadvantages, such as the challenge of correcting for the effects of temperature on measurements and the high fragility of the fiber, which requires large curvature radii to limit signal loss or attenuation. In this work, fiber bragg gratings (FBG) sensors are used. They are produced in the fiber by periodically changing the core refractive index using a laser technique. There are some core bands with a modified refractive index in a fiber trait of about 1 cm at the conclusion of this operation. Each of the bands with the modified refractive index is separated by a particular distance, which is known as *grating period* $\Lambda_G$. When the light crosses through it, the sensor is able to reflect a certain wavelength called *Bragg frequency*, described by the following equation:

$$\lambda_B = 2n_{eff}\Lambda \tag{3}$$

where $\lambda_B$ is the wavelength reflected by the FBG, $n_{eff}$ is the refractive index of the fiber (after the remodulation), $\Lambda_G$ is the pitch of the grating as shown in Figure4. The sensor output is represented by the Bragg frequency.

The relationship between the Bragg frequency and the grating pitch, which is a measure of physical distance, is seen in equation 3. This implies that the mechanical strain caused by an external component on the grating period, which causes the variation in the reflected wavelength, is always connected. Because of this, the FBG can detect a change in the Bragg wavelength brought on by a variety of factors (mechanical deformation, temperature, humidity), but it cannot, at least initially, quantify the various contributions. The effect of temperature and humidity on the precision of the mechanical deformation measurements of the FBG can be expected to be minor in the situation of constant temperature and humidity (or defined by very small changes or extremely slow temporal evolutions).
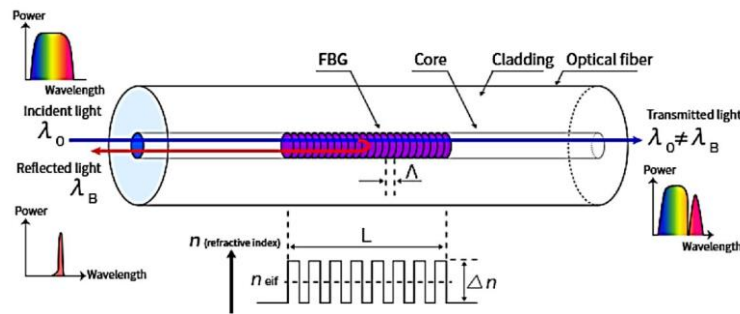

Figure 4: FBG working principle

On the other hand, if multiple parameters experience large alterations, it is important to analyze how these changes affect FBG measurements and develop a suitable strategy for filtering the raw results returned by the optical sensor. Therefore, it is crucial to develop a successful compensatory technique when using FBGs as mechanical strain sensors.

The general variation of the reflected wavelength $\lambda_B$ can be expressed as follows:

$$\Delta\lambda_B = \lambda_B(1 + p_E)\Delta\varepsilon + (\alpha_\Lambda + \alpha_n)\Delta T \tag{4}$$

- $\lambda_B$ is the nominal reflected wavelength;
- $p_e$ is the strain-optic or photoelastic coefficient of the fiber;
- $\Delta\varepsilon$ is the variation of fiber strain;
- $\alpha_\Lambda$ is the thermal expansion coefficient of the fiber;
- $\alpha_n$ is the thermo-optic coefficient of the fiber;
- $\Delta T$ is the variation of the temperature;

Equation 4 can be reformulated as:

$$\Delta\lambda_B = K_\varepsilon\Delta\varepsilon + K_T\Delta T \tag{5}$$

where the terms $K_\varepsilon = (1 + p_E)$ and $K_T = (\alpha_\Lambda + \alpha_n)$ are defined as *coefficient of strain* and *coefficient of temperature*, respectively. These coefficients are derived considering an optical fiber which is stressed but not bonded to other materials. More specifically, $K_\varepsilon$ is a function of the strain-optic coefficient: it depends from the material of the fiber and describes the variation of the refraction index induced by a normal stress.

Instead, the $K_T$ is composed by two different contributes:

- the thermos-optic coefficient $\alpha_n$ which represents the variation of the refraction index caused by the temperature
- the thermal expansion coefficient $\alpha_\Lambda$, which is related to the effect of temperature on the physical disposition of the Bragg grating.

## 2.1 Definition of test campaign

This work experimentally analyzes the possibility of simultaneous monitoring of temperature and mechanical strain using different configurations of optical sensors. All the sensors were mounted on specimens which have been designed to simulate, as a first approximation, the behavior of a flexed wing during a flight phase.
In this regards, a multiple steps test campaign has been defined:

1. Thermal calibration of the developed sensors.
2. Mechanical calibration of the developed sensors
3. Verification of the FBG sensitivity to mechanical loads even when strongly thermally perturbed.

More in details, the thermal compensation applied in the second phase of the campaigns has been realized following different strategies:

- In the first phase, the sensor is placed in a climatic chamber, thermally perturbed, and subjected to a mechanical load. The filtering of the thermal contribution is performed using temperature information from an electronic sensor.
- In the second phase, the thermal-mechanical contributions are distinguished using only FBG optical sensors. A second specimen is then realized and only employed for thermal measures. Instead, the ancient one, put in the same environment but also mechanically stressed, is used to measure the loads-induced strain.
- Finally, a preliminary study is provided for further implementation of the second method. In particular, thanks to the presence of several sensors on the same specimen, a proposal of thermal mechanical decoupling while using only the stressed specimen is described.

The thermal compensation activity is realized remembering the general equation of an FBG:

$$\Delta\lambda_B = K_\varepsilon\Delta\varepsilon + K_T\Delta T \tag{6}$$

Where $\Delta\lambda$ is directly measured by the test bench, $K\varepsilon$ and $KT$ are calculated during calibration phase, while $\Delta T$ is provided or by an electronic sensor by a second FBG not mechanically stressed as

$$\Delta T = \frac{\Delta\lambda_B}{K_T} \tag{7}$$

Instead, for the last strategy two sensors are combined in order to obtain the following linear system:

$$\begin{Bmatrix} \Delta\lambda_1 \\ \Delta\lambda_2 \end{Bmatrix} = \begin{bmatrix} K_{\varepsilon 1} & K_{T1} \\ K_{\varepsilon 2} & K_{T2} \end{bmatrix} \begin{Bmatrix} \Delta\varepsilon \\ \Delta T \end{Bmatrix} \tag{8}$$

Where:

- $K_\varepsilon$ and $K_T$ other than being the unknowns of the problem, represent the strain and temperature changes to which both sensors are subjected.
- $K_{\varepsilon 1,2}$ and $K_{T1,2}$ are the strain and temperature coefficients.
- $\Delta_{\lambda 1,2}$ represents the wavelength shift to which the FBGs are subjected.

## 2.2 Experimental test bench

As previously mentioned, two samples that have the identical rectangular shape (260x35x1.6 mm) and are made of 14 layers of unidirectional carbon fiber were constructed. They were sliced from a single block of composite material that contained *Tenax UTS 50* carbon fiber and Cytox "*Epoxi ResinL*" as a matrix. The first sample, referred to as "Specimen 1," has one optical line with one FBG installed along the elastic axis (in the centerline) and about midway down. During the bonding stage, this optical line was pre-loaded or pre-stretched. The bonding phase was broken down into the following stages::

1. Positioning and clamping of the specimen on two 3D-printed supports, anchored to an optical breadboard.

2. Positioning of the fiber and FBG sensor in the desired position.
3. Initial fixing of one end of the fiber: by means of adhesive tape on the portion of the fiber equipped with a heat-shrink sleeve and by means of cyano-acrylic glue on a portion immediately downstream.
4. Anchoring the free end of the fiber to a plate, which is constrained on a linear-translator.
5. Pre-loading the fibre by translation of the linear-translator.
6. Deposition of an epoxy resin layer over the entire line.
7. Wait for the end of the resin curing process.
8. Release and cut of the free extreme.
9. Gluing a strain gauge near the FBG.

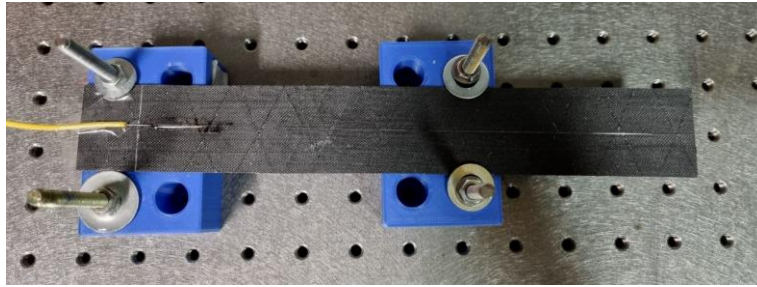In figure there is a the specimen with the fiber before being glued on it.


Figure 5: specimen 1 preparation

The second sample, called "*Specimen 2* ", shares the same dimensions of the previous one, and is equipped with 2 optical lines, each containing 2 FBGs of 1546 and 1538 [nm] nominal Bragg wavelength. Both lines are symmetrically placed with regard to the central axes (elastic axes). As a peculiarity, only one optical line is pre-loaded (3500 $\mu\varepsilon$). The bonding and pre-loading procedure is the same as for Specimen 1. The second line, instead, is simply placed on the specimen and then bonded with epoxy resin. As can be seen from the picture, the sample has also a circular hole at a free end, approximately in the elastic axes, which will be useful for applying a load and conduct bending tests.
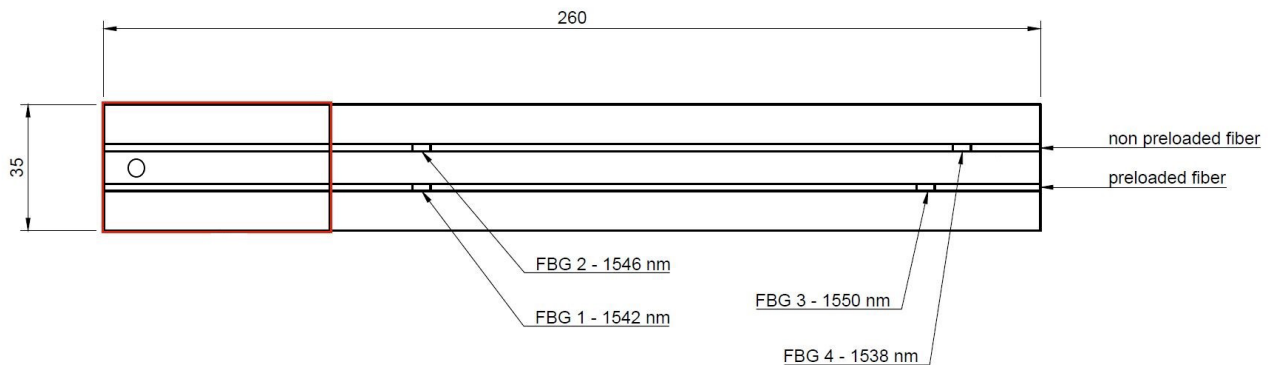

Figure 6: scheme of specimen 2

Temperature is crucial in the thermomechanical calibration phase, thus an instrument that allows its values to be monitored and controlled has taken on a major role in carrying out the experimental tests: the climatic chamber. The one utilized in this experiment is the Kambic KK-50CHLT model, which allowed both specimens (Specimen 1 and Specimen 2) to be housed inside it, allowing them to be varied and/or maintained to a desired temperature in order to complete the required tests. Table 1 summarizes the instrument's properties.

It is critical to know the value at well-defined intervals, whether they are one second or a few minutes, for doing time-varying temperature tests as well as constant-temperature testing. This project made use of a Sensirion SHT85 sensor, which can measure both temperature and humidity. It must be interfaced to a microcontroller, such as an Arduino UNO in our case, which is then connected via USB cable to a computer in order to read the output values. Figure 7 depicts the wiring diagram between the SHT85 sensor and the Arduino UNO microcontroller.

Table 1: climatic chamber specifics

**KK 50**

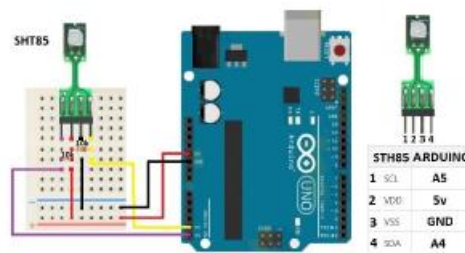| | |
|---|---|
| External dimensions | 570x1035x645 mm |
| Internal dimensions | 400x375x350 mm |
| Volume | 50L |
| Temperature range | -40; +180°C |
| Temperature resolution | 0.1 °C |



Figure 7. Temperature sensor and Arduino

Furthermore, a specifically created code must be placed into the microcontroller board via a PC in order for it to function. This script prints the temperature (and, if needed, humidity) value measured by the sensor at predefined time intervals, such as one second, to the serial display. Following completion of the measurement, the serial monitor data can be recorded in a ".txt" file and made available for post-processing. Instead, the strain gauge was driven by an HBM QuantumX MX1615B control unit, which served as an interface between the sensor and the computer during the strain tests. Data was collected using HBM's catman®Easy program, with the acquisition frequency set to 20 Hz, which was as near to the FBG sensor one (25Hz) as possible.

Finally, the technique for acquiring data generated by FBG sensors (in terms of reflected wavelength) involves only two components: a computer and an optical interrogator. The optical interrogator is a device that can both emit a light signal and receive reflected signals from gratings. The instrument employed in this study is a SmartScan from SmartFibres, which is a Wavelength Division Multiplexing (WDM) device with an agile, tuneable laser source that allows for high-resolution interrogation at multi-kHz frequencies.
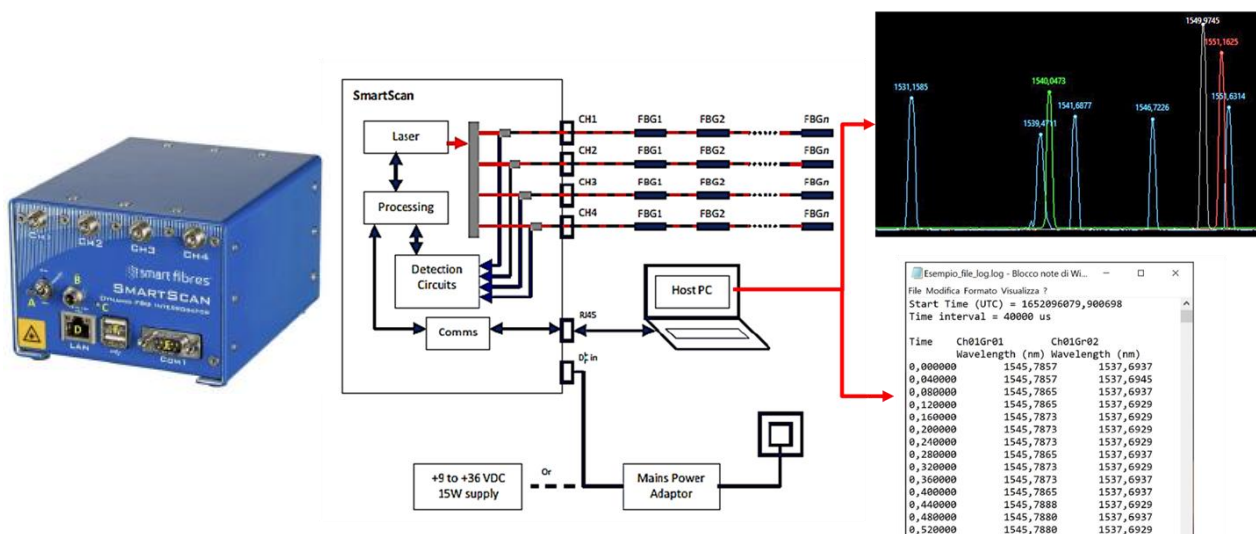


Figure 8: FBG data acquisition system

The interrogator requires both electrical power and a LAN connection to be interfaced with a computer. The computer must have the Smartfibres software installed. The software's main screen displays a real-time graph depicting the fiber's response, specifically the intensity and wavelength of the peaks generated by the signal reflected by the FBG sensors. In the top-left corner, you can select the number of channels and the corresponding number of fibers to be used. Additionally, you can specify the number of sensors per channel. From this screen, you can also configure other parameters such as the acquisition frequency, the intensity threshold for peak detection, the sampling interval size, and the transmission frequency.

The output file generated by the software is a text file containing the wavelength values of the individual peaks corresponding to each FBG sensor, recorded at each sampling time interval. These files were subsequently imported into Matlab for further post-processing operations. Once the data acquisition from the SmartScan and the SHT85 is complete, the post-processing phase begins.

The interrogator's output is represented by a '.log' file, which contains the following information:

- In the first two lines are reported the acquisition start time and the time intervals between two measurements. In our case, for a 25 Hz acquisition frequency, the time interval is 40000 $\mu s$.
- A column division starts from the fourth line. The same line shows the names of the sensors detected, and in the first column the 'Time' entry indicating the acquisition time
- Finally, the data acquired by each sensor at the specific time instant are saved beginning with the sixth line.

The SmartScan interrogator has the capability to read up to 4 optical channels, each accommodating up to 16 sensors. The output file organizes the sensors based on their corresponding channels and assigns a numerical index to each sensor according to its wavelength. For instance, the FBG sensor connected to the first channel with the longest wavelength will be labeled as Ch01Gr01, while the sensor with the next shortest wavelength will be denoted as Ch01Gr02. This sorting scheme disregards the spatial arrangement of the sensors and focuses solely on their wavelengths.Once the file handling process is clear, the data can be processed. For this purpose, specific Matlab scripts have been developed for each type of experimental test. These scripts enable the reading and processing of files generated by both the interrogator and the Arduino, depending on the specific objectives of the test. The wavelengths, elapsed time since the start of the acquisition, and the names of each FBG sensor are saved in a structure, while the temperature data from the SHT85 is stored in a vector for convenient access.

## 3. Experimental campaign

This section describes the experimental procedure for thermal calibration, mechanical calibration and mixed thermo-mechanical stress testing.

### 3.1. Thermal calibration

The thermal characterisation entails determining the FBG's KT coefficient by a direct link between wavelength variation and temperature variation.

If the FBG is not susceptible to mechanical deformation, i.e. if the applied load is zero, this approach is feasible. In fact, if no load is given to the sample, equation 4.1 looks like this:

$$\Delta\lambda_B = K_T\Delta T \tag{9}$$

And since the $\Delta T$ is known from the temperature sensor, as is the $\Delta\lambda B$ from the SmartScan, it is immediate to determine the $K_T$. The experimental activity was carried out according to the following steps:

- Setting up Specimen 1 on a flat surface inside the climatic chamber
- Connecting the FBG with the SmartScan
- Positioning the SHT85 sensor in close proximity to the FBG, in order to capture as accurately as possible the same temperature perceived by the optical sensor
- Setting the temperature interval in the climatic chamber and its rate of change (°C/h)
- Simultaneous start of the climate chamber cycle and the acquisition of the temperature and the FBG wavelengths
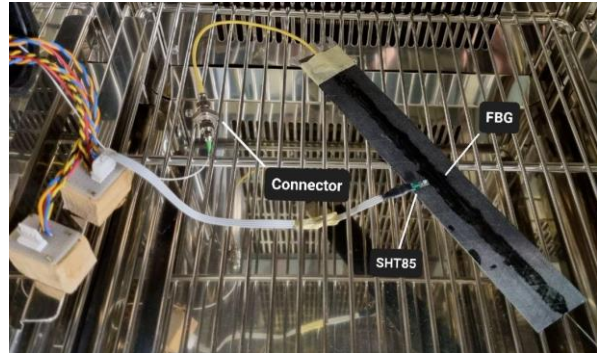- End of acquisitions and temperature cycle
- Data storage and post-processing

Figure 9: Setup for thermal characterization

The thermal characterization was performed in the temperature range from -40°C to +40 °C. Figure 10 shows the evolution of the wavelengths as a function of temperature.
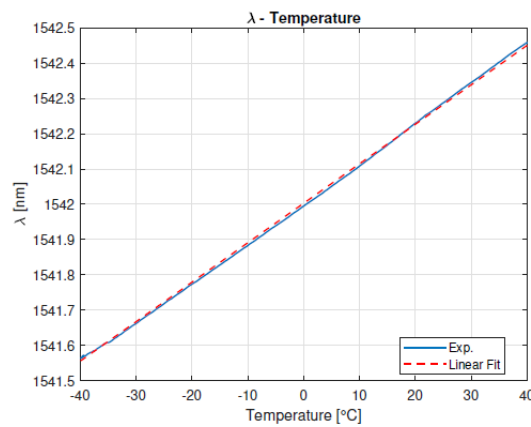

Figure 10: FBG calibration curve

This graphic clearly shows a linear relationship between what the FBG sensor measures and the temperature. The $K_T$ coefficient and the wavelength corresponding to 0°C, denoted as 0, can be calculated using linear interpolation. The values calculated from the linear fit are reported in table 2.

Table 2: linear fit parameters for thermal calibration

**Specimen 1**

| | |
|---|---|
| $K_T$ | 0.0112 |
| $\lambda_0$ | 1542.0028 |

Thanks to this calibration, it is possible to estimate the temperature perceived by the FBG as:

$$T = \frac{\lambda_m - \lambda_0}{K_T}$$ (10)

and compare it with the real value directly sensed by the SHT85. In fact, a *Root Mean Square Error (RMSE)* of 0.007 has been calculated from the linear fit of the experimental data.

## 3.2. Mechanical calibration

To use the FBG sensor 1 as a mechanical strain sensor, you must understand not only the temperature and the corresponding coefficients 0 and KT, but also the K coefficient. The strategy is to perform bending load tests with a strain gauge to measure the deformation of the FBG sensor as a function of the applied load. Knowing that only pure-bending load tests will be performed, it was chosen to attach a single strain gauge next to the FBG sensor to measure

the (nearly) same deformations as the optical sensor. The sensor installation technique is outlined in the following steps:

- Identification of the optimal sensor location.
- Cleaning of the installation surface.
- Adhesive gluing of the sensor with a specific glue.
- Wire soldering.
- Application of a protective layer of epoxy resin.
- Setting up the connection to the control unit.

The test comprises of 5 distinct load stages (0, 85, 180.2, 275.4, 376.4 [g]) applied at a constant temperature. It is feasible to know the temperature and remove its effect from the overall contribution by positioning the SHT85 sensor near the FBG. Once the is known, i.e. the relative contribution to mechanical deformation, the deformations registered by the strain gauge ($\Delta\lambda_\varepsilon$) for each load step can be used to find a correlation between and the relative deformation. The $K_\varepsilon$ coefficient can then be calculated using the following relationship::

$$K_\varepsilon = \frac{\Delta\lambda_B - \Delta\lambda_T}{\Delta\varepsilon} \qquad (11)$$
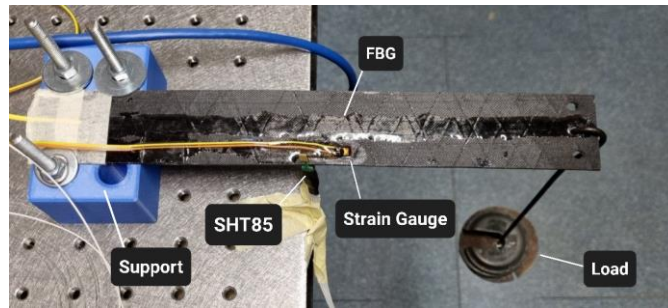
The test setup is shown in figure 11.



Figure 11: Specimen1 setup for bending test with strain gauge

Figure 12 depicts the relationship between the mechanical contribution $K_\varepsilon$ and the strain recorded by the strain gauge. A dashed straight line represents the data produced by a linear interpolation between those quantities. A comparison of the two curves, experimental and interpolated, reveals that there are no discernible differences. A Root Mean Square Error (RMSE) of 0.0126 confirms the linearity of the relationship between the two values. This pattern demonstrates that the $K_\varepsilon$ remains constant as a function of strain. This property justifies the inclusion of the $K_\varepsilon$ coefficient as a consequence of linear interpolation.
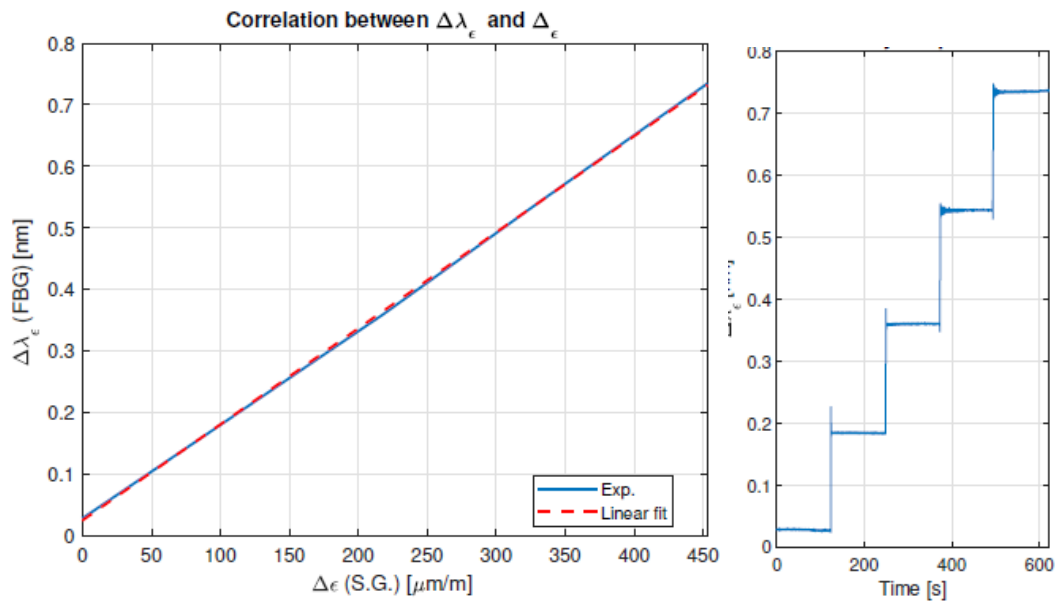


Figure 12: Mechanical calibration and FBG output

Once the value of K$\varepsilon$ is determined, the strain measured by the FBG sensor can be calculated. A graphical comparison between the strain trend obtained from the FBG sensor and the strain gauge reveals a close resemblance in the results. However, the strain trend measured by the optical sensor appears to be more stable compared to that of the strain gauge. Since a static load test was conducted, where the applied load remained constant over time, it would be expected to observe constant deformations for each load step after the initial oscillatory phase. The strain trend observed from the FBG sensor aligns more closely with this expected behavior, indicating its higher reliability compared to the strain gauge.

Furthermore, Figure 14 illustrates the relationships between load, wavelength, and strain. It is worth noting that there is a difference in the slope between the two curves, which can be attributed to the presence of the K$\varepsilon$ coefficient.
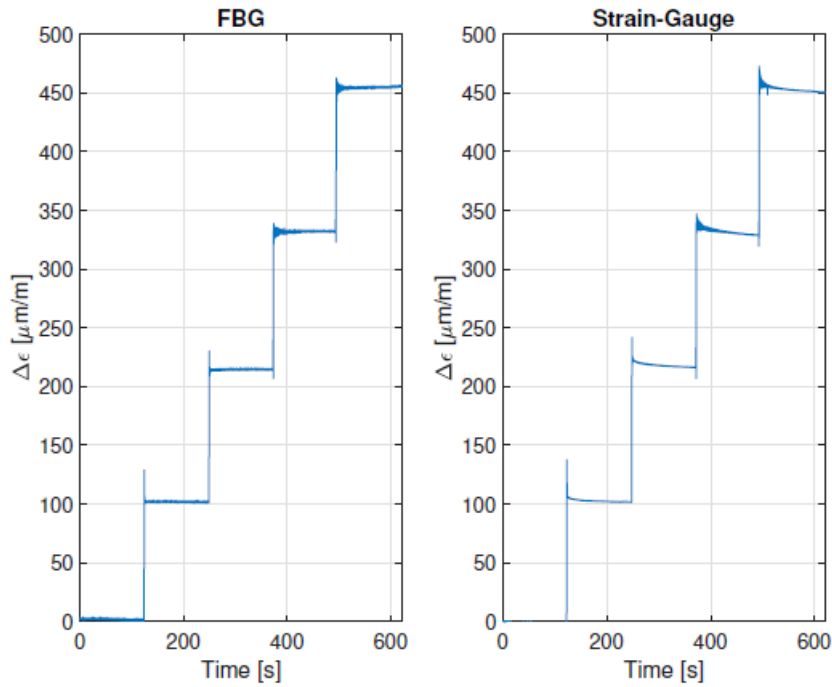


Figure 13: comparison between FBG and strain gauge data.
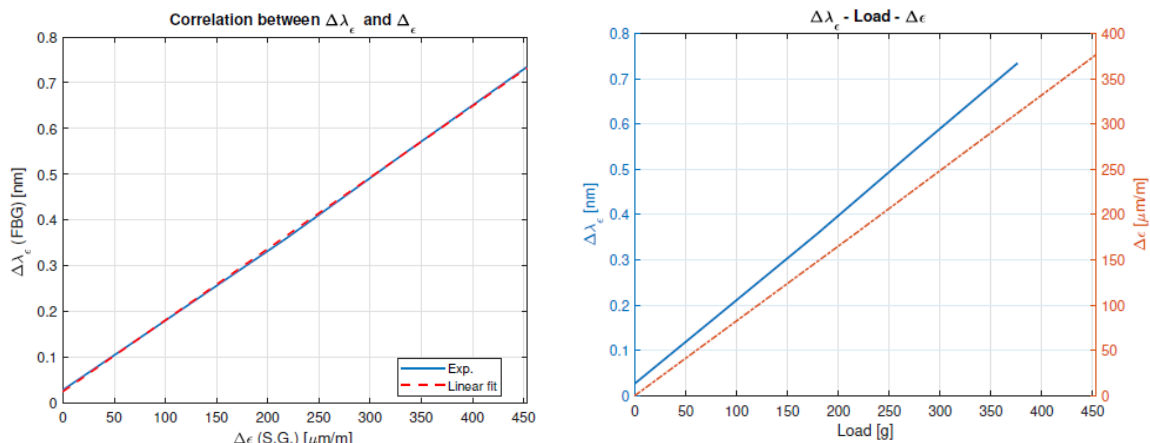


Figure 14: final mechanical FBG calibration.

## 3.2. Thermo-mechanical decoupling test

The final part of the test consists in a multiple parameters data acquisition. The system is put inside the climatic chamber and both exposed to a step-increasing load and a thermal cycle. Two different thermal cycles were applied:

- FBG in load test at variable temperature with a slope of 30°C/h
- FBG in load test at variable temperature with a slope of 60°C/h

The overall test was replicated three times for the three different compensation strategies:

- one specimen with electronic temperature sensor;
- two specimens for the optical compensation strategy;
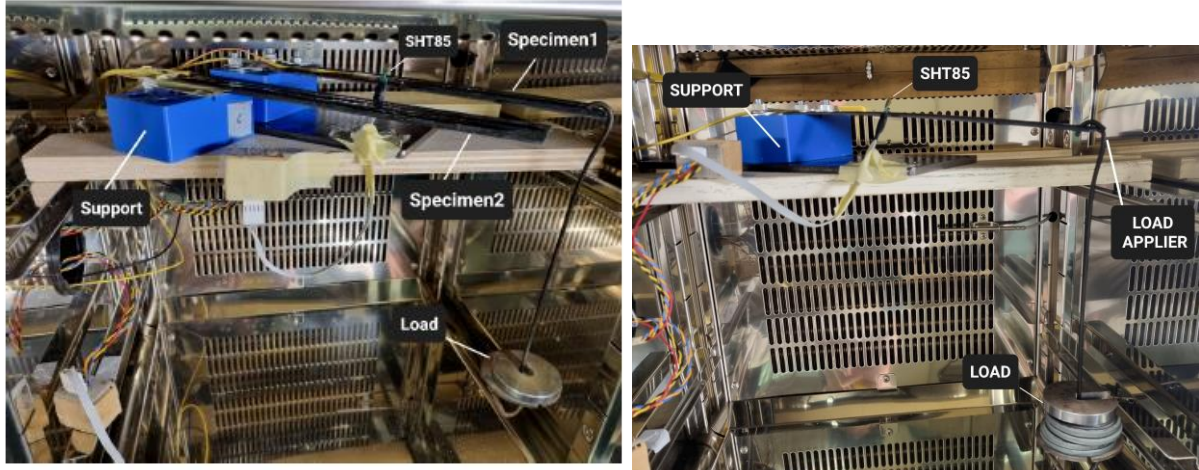- one specimen with multiple FBGs for the in situ compensation.
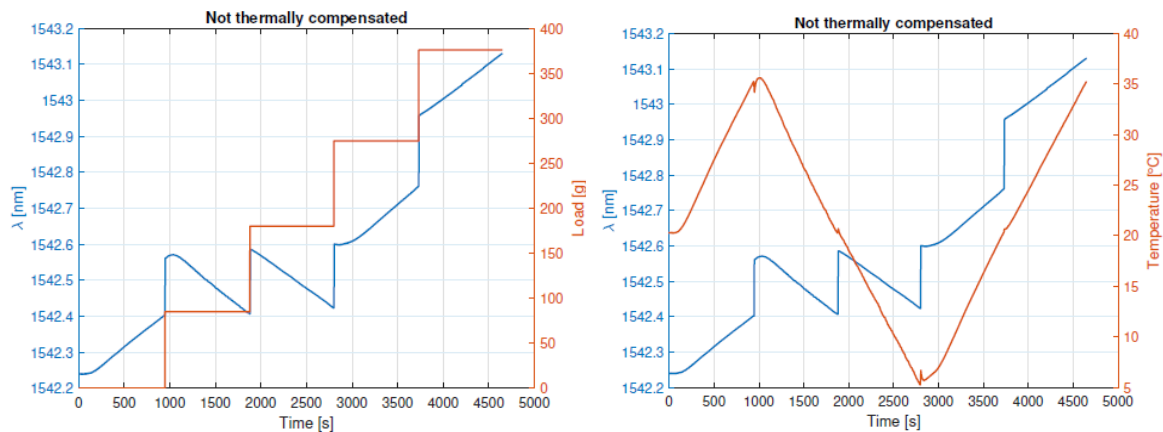


Figure 15: setup of test with two and one specimen.



Figure 16: applied loads and optical data

## 4. Results and discussion

The analysis of thermo-mechanical decoupling focuses on evaluating different strategies of thermal compensation. Initially, temperature data from the SHT85 sensor is used for this purpose. The results are presented in the graph shown in Figure 17 and summarized in the accompanying table 3. The maximum absolute difference occurs during the second load step, reaching 12 [μm/m], which corresponds to approximately a 5% relative difference. These findings indicate a consistent agreement between the results obtained.

Based on these results, it can be concluded that the thermomechanical decoupling strategy enables the FBG sensor to provide reliable measurements of both temperature and mechanical strain. However, a noteworthy observation arises when comparing the experimental results with the expected theoretical values for the strain coefficient $K\varepsilon$.
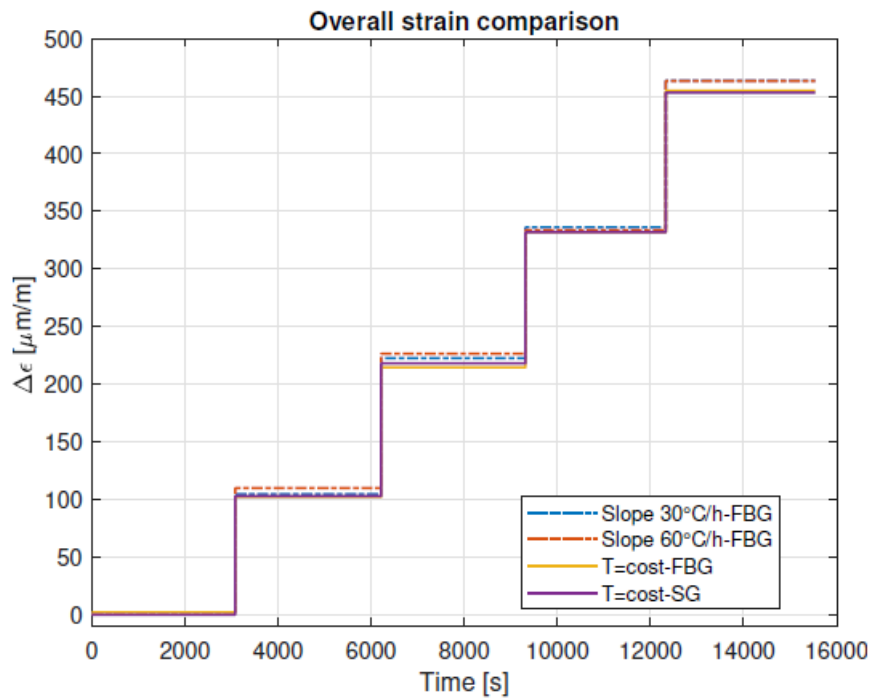
11

Figure 17: data comparison after contributes decoupling

Table 3. Data comparison

**Specimen 1: Δε [μm/m]**

| Load$_T$ | SG | FBG | FBG 30°C/h | FBG 60°C/h |
|---|---|---|---|---|
| **0 g** | -0.44 | 1.80 | 0 | 0 |
| **85 g** | 102.63 | 101.99 | 104.54 | 109.51 |
| **180.2 g** | 217.98 | 214.5 | 222.52 | 226.34 |
| **275.4 g** | 331.84 | 332.03 | 335.88 | 333.57 |
| **376.4 g** | 453.06 | 454.74 | 463.48 | 463.27 |

For the second technique, which is entirely optical thermal compensation, the performance of temperature sensors is first evaluated. As shown in figure 18, two of the four temperature sensors are genuinely coherent with data from the electronic probe, while the other two indicate a more considerable inaccuracy, most likely due to the farthest positioning in the experimental set-up. This is clearly resumed by the RMSE numbers presented in table 4.
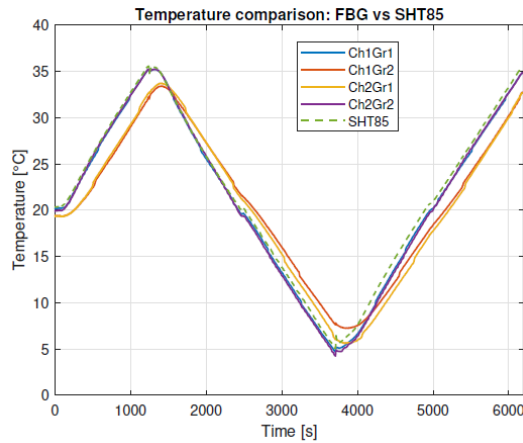
THERMOMECHANICAL CALIBRATION OF FBG SENSORS FOR AEROSPACE APPLICATIONS



Figure 18: thermal compensation accuracy comparison

Table 4. data comparison

**Temperature comparison**

|  | **Ch1Gr1** | **Ch1Gr2** | **Ch2Gr1** | **Ch2Gr2** |
|---|---|---|---|---|
| **RMSE** | 0.6261 | 2.452 | 2.4868 | 0.7564 |

So, data coming from the two best sensors are employed for thermal compensate the strain FBG sensor. The results are showed in figure. Finally, this optical-only system proved the feasibility of thermomechanical decoupling using only optical sensors, but at the same time highlighted the importance to carry out a reliable thermal characterization.
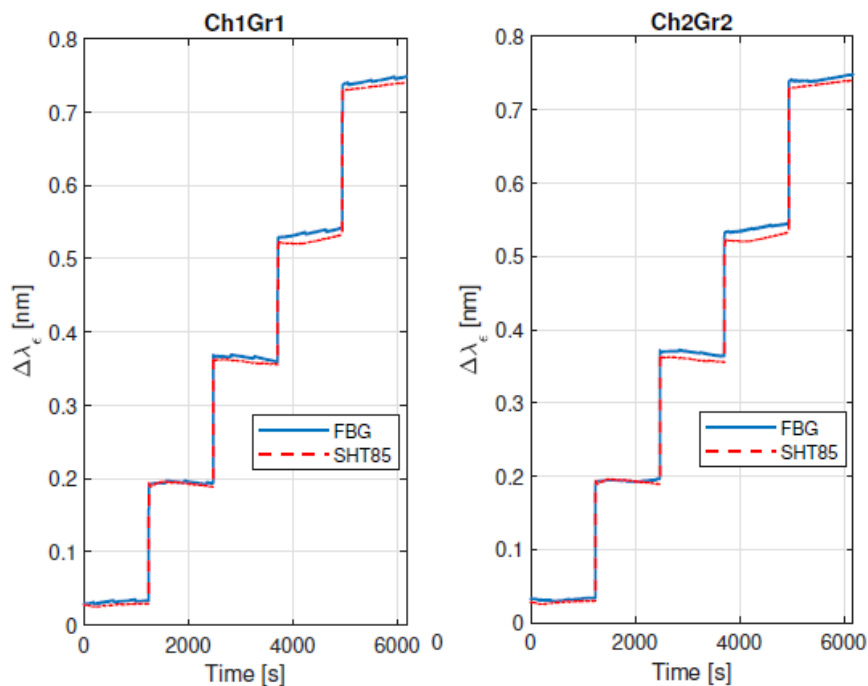


Figure 19: final comparison after decoupling.

When comparing the experimental results to the theoretical value, it is observed that the Kε coefficient exhibits a 28% increase. The findings presented in Figure 19 indicate that the Kε coefficient remains constant regardless of the applied load, suggesting that a similar value would be expected between the theoretical coefficient (determined under unloaded fiber conditions) and the experimental one. However, it should be noted that the reference value pertains to an optical sensor that is not installed on any surface or pre-loaded, which may justify this difference.

Nevertheless, it is important to consider that other factors could contribute to this variation. One possibility is the imperfect alignment between the FBG sensor and the strain gauge, causing the digital sensor to measure a greater strain compared to the optical sensor. Another plausible hypothesis is the presence of torsion and bending in addition to pure bending in the specimen. In such a scenario, since the strain gauge is positioned at a non-zero distance from the FBG sensor, it may measure a strain component that differs from that detected by the FBGs.

Finally, an analysis is presented for the results obtained using the last approach. Figure 4.50 displays the time-evolution of the reference temperature (SHT85) and the temperature resulting from solving the linear system. It can be observed that the results exhibit a high level of inaccuracy, as indicated by the Root Mean Square Error (RMSE) of 11.0309 between the two trends. Similar conclusions can be drawn for the mechanical strain, as shown in Figure 4.51, which includes the evolution of the applied load. Based solely on the analysis of the obtained results, it can be concluded that the thermal decoupling strategy based on an optical-only system fails to achieve proper decoupling between the two phenomena.

However, it is important to note that the obtained results are influenced by the overlapping of errors of various nature. Specifically, the thermal characterization revealed a degradation in the quality of the results provided by the FBGs of Specimen2 compared to Specimen1, which inevitably impacted the determination of the strain coefficients. Consequently, since the linear system 4.8 is highly dependent on the $K\varepsilon$ and $KT$ coefficients, it leads to unreliable results. Despite the presence of a significant error, it can be observed from Figure 20 that the trends exhibit a temporal evolution that somewhat resembles the actual trend. The temperature trend slightly resembles that of the SHT85, and similarly, the temporal evolution of the mechanical strain follows an overall increasing trend, consistent with the applied load.

Based on these considerations, it is believed that the thermomechanical decoupling strategy relying solely on a single optical system may be capable of achieving correct decoupling between the thermal and mechanical phenomena. However, it requires a high level of accuracy in determining the temperature and strain coefficients. Therefore, a new purely-optical configuration should be developed with the aim of minimizing the margin of error and demonstrating the feasibility of this approach.
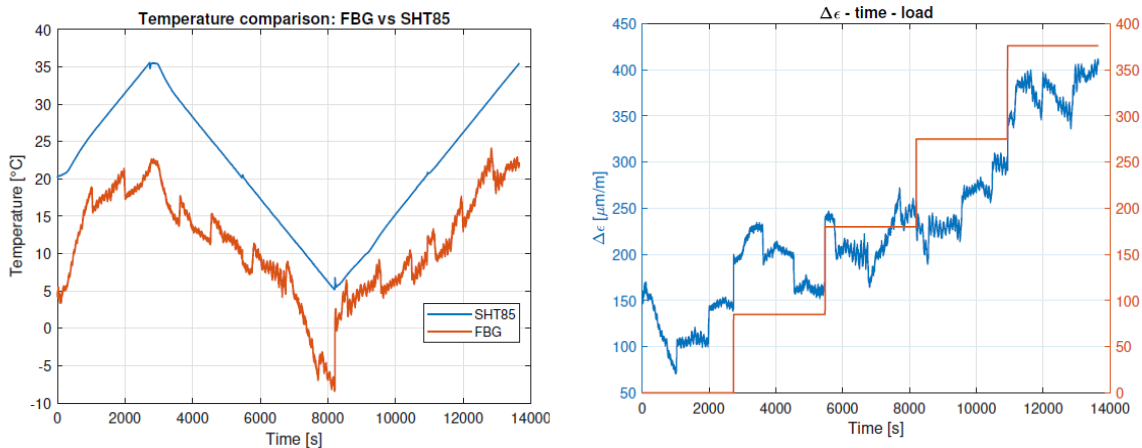


Figure 20: data comparison with last strategy.

## 4. Conclusions

In this work is discussed the validation of a thermomechanical decoupling methodology that can guarantee a concrete implementation possibility of FBG sensors on composite material structures. The presented solutions succeeded in decoupling thermal and mechanical phenomena, either through the use of a mix of optical and digital sensors, or through exclusively optical sensors. Depending on the type of application, the diversity of the proposed approaches allows a high degree of flexibility and the possibility of choosing the sensor configuration that best suits to the needs. In particular, an optical-digital system is the easiest approach to implement, and guarantees excellent results in terms of decoupling . Similarly, it has been verified that a system composed exclusively of optical sensors mounted on two mechanically-decoupled structures, one of which is not subject to mechanical deformation, can also lead to excellent results. The last system, on the other hand, which is completely optical and installed on a single structure, was not able to provide sufficiently reliable results at the moment, due to specific uncertainties that shall be overcome.

In conclusion, the excellent possibility of decoupling different contributes from the overall optical FBG output is demonstrated. Next tests will allow to define a best practice for increasing data confidence.

# References

[1]     Safa. Kasap, *Optoelectronics and photonics : principles and practices*. Prentice Hall, 2001.

[2]     R. Rodríguez-Garrido *et al.*, "High-temperature monitoring in central receiver concentrating solar power plants with femtosecond-laser inscribed fbg," *Sensors*, vol. 21, no. 11, Jun. 2021, doi: 10.3390/s21113762.

[3]     S. J. Mihailov, "Fiber Bragg Grating Sensors for Harsh Environments," *Sensors*, vol. 12, pp. 1898–1918, 2012, doi: 10.3390/s120201898.

[4]     S. J. Mihailov *et al.*, "Extreme Environment Sensing Using Femtosecond Laser-Inscribed Fiber Bragg Gratings", doi: 10.3390/s17122909.

[5]     G. P. Agrawal and S. Radic, "Phase-Shifted Fiber Bragg Gratings and their Application for Wavelength Demultiplexing," *IEEE Photonics Technology Letters*, vol. 6, no. 8, pp. 995–997, 1994, doi: 10.1109/68.313074.

[6]     S. J. Mihailov *et al.*, "Ultrafast laser processing of optical fibers for sensing applications," *Sensors*, vol. 21, no. 4. MDPI AG, pp. 1–23, Feb. 02, 2021. doi: 10.3390/s21041447.

[7]     A. Behbahani, M. Pakmehr, and W. A. Stange, "Optical Communications and Sensing for Avionics," in *Springer Handbooks*, Springer Science and Business Media Deutschland GmbH, 2020, pp. 1125–1150. doi: 10.1007/978-3-030-16250-4_36.

[8]     A. C. Marceddu *et al.*, "Air-To-Ground Transmission and Near Real-Time Visualization of FBG Sensor Data Via Cloud Database," *IEEE Sens J*, 2022, doi: 10.1109/JSEN.2022.3227463.

[9]     A. Aimasso, M. D. L. D. Vedova, and P. Maggiore, "Innovative sensor networks for massive distributed thermal measurements in space applications under different environmental testing conditions," in *2022 IEEE 9th International Workshop on Metrology for AeroSpace, MetroAeroSpace 2022 - Proceedings*, 2022. doi: 10.1109/MetroAeroSpace54187.2022.9856275.

[10]    A. Aimasso, M. D. L. Dalla Vedova, P. Maggiore, and G. Quattrocchi, "Study of FBG-based optical sensors for thermal measurements in aerospace applications," in *Journal of Physics: Conference Series*, 2022. doi: 10.1088/1742-6596/2293/1/012006.

[11]    M. D. L. Dalla Vedova, P. C. Berri, and A. Aimasso, "Environmental sensitivity of Fiber Bragg Grating sensors for aerospace prognostics," in *Proceedings of the 31st European Safety and Reliability Conference, ESREL 2021*, 2021. doi: 10.3850/978-981-18-2016-8_634-cd.

[12]    R. E. Quigley, "More Electric Aircraft," *Proceedings Eighth Annual Applied Power Electronics Conference and Exposition,* pp. 906–911, 1993, doi: 10.1109/APEC.1993.290667.

[13]    Z. Yin, N. Hu, J. Chen, Y. Yang, and G. Shen, "A review of fault diagnosis, prognosis and health management for aircraft electromechanical actuators," *IET Electr Power Appl*, vol. 16, no. 11, pp. 1249–1272, Nov. 2022, doi: 10.1049/ELP2.12225.

[14]    D. Belmonte, M. D. L. Dalla Vedova, and P. Maggiore, "Prognostics of onboard electromechanical actuators: A new approach based on spectral analysis techniques," *International Review of Aerospace Engineering*, vol. 11, no. 3, pp. 96–103, 2018, doi: 10.15866/irease.v11i3.13796.

[15]    T. L. Yeo, T. Sun, K. T. V. Grattan, D. Parry, R. Lade, and B. D. Powell, "Characterisation of a polymer-coated fibre Bragg grating sensor for relative humidity sensing," *Sens Actuators B Chem*, vol. 110, no. 1, pp. 148–156, Sep. 2005, doi: 10.1016/J.SNB.2005.01.033.

[16]    B. Gu, A. P. Zhang, M. Yin, J. Qian, and S. He, "Optical fiber relative humidity sensor based on FBG incorporated thin-core fiber modal interferometer," *Optics Express, Vol. 19, Issue 5, pp. 4140-4146*, vol. 19, no. 5, pp. 4140–4146, Feb. 2011, doi: 10.1364/OE.19.004140.

[17]    V. Rao Pachava, S. Kamineni, S. Shankar Madhuvarasu, and K. Putha, "A high sensitive FBG pressure sensor using thin metal diaphragm", doi: 10.1007/s12596-014-0186-9.

[18]    H. Wang, S. Li, L. Liang, G. Xu, and B. Tu, "Fiber grating-based strain sensor array for health monitoring of pipelines," *SDHM Structural Durability and Health Monitoring*, vol. 13, no. 4, pp. 347–359, 2019, doi: 10.32604/sdhm.2019.05139.

[19]    V. de Miguel-Soto *et al.*, "Study of optical fiber sensors for cryogenic temperature measurements," *Sensors (Switzerland)*, vol. 17, no. 12, 2017, doi: 10.3390/s17122773.

[20]    F. Attivissimo, F. Adamo, L. De Palma, D. Lotano, and A. Di Nisio, "First experimental tests on the prototype of a capacitive oil level sensor for aeronautical applications," *Acta IMEKO*, vol. 12, no. 1, pp. 1–6, Feb. 2023, doi: 10.21014/ACTAIMEKO.V12I1.1474.

[21]    S. De Gioia, F. Adamo, F. Attivissimo, D. Lotano, and A. Di Nisio, "A design strategy for performance improvement of capacitive sensors for in-flight oil-level monitoring aboard helicopters," 2023, doi: 10.1016/j.measurement.2023.112476.